MAJOR ARTICLE

Mycobacterium tuberculosis HN878 Infection Induces Human-Like B-Cell Follicles in Mice

José Alberto Choreño-Parra,[1,2] Suhas Bobba,[1] Javier Rangel-Moreno,[3] Mushtaq Ahmed,[1] Smriti Mehra,[4,5,6] Bruce Rosa,[7] John Martin,[7] Makedonka Mitreva,[7] Deepak Kaushal,[4,8,9] Joaquín Zúñiga,[10] and Shabaana A. Khader[1]

[1]Department of Molecular Microbiology, Washington University School of Medicine in St. Louis, St. Louis, Missouri, USA, [2]Escuela Nacional de Ciencias, Instituto Politécnico Nacional, Mexico City, Mexico, [3]Division of Allergy/Immunology and Rheumatology, University of Rochester School of Medicine and Dentistry, Rochester, New York, USA, [4]Tulane National Primate Research Center, Tulane University School of Medicine, Covington, Louisiana, USA, [5]Department of Pathobiological Sciences, Louisiana State University School of Veterinary Medicine, Baton Rouge, Louisiana, USA, [6]Center for Experimental Infectious Disease Research, Louisiana State University School of Veterinary Medicine, Baton Rouge, Louisiana, USA, [7]Department of Medicine, Washington University in St. Louis School of Medicine, St. Louis, Missouri, USA, [8]Division of Bacteriology and Immunology, Tulane National Primate Research Center, Covington, Louisiana, USA, [9]Southwest National Primate Research Center, Texas Biomedical Research Institute, San Antonio, Texas, USA, [10]Laboratory of Immunobiology and Genetics, Instituto Nacional de Enfermedades Respiratorias "Ismael Cosío Villegas," Mexico City, Mexico

Specific spatial organization of granulomas within the lungs is crucial for protective anti-tuberculosis (TB) immune responses. However, only large animal models such as macaques are thought to reproduce the morphological hallmarks of human TB granulomas. In this study, we show that infection of mice with clinical "hypervirulent" *Mycobacterium tuberculosis (Mtb)* HN878 induces human-like granulomas composed of bacilli-loaded macrophages surrounded by lymphocytes and organized localization of germinal centers and B-cell follicles. Infection with laboratory-adapted *Mtb* H37Rv resulted in granulomas that are characterized by unorganized clusters of macrophages scattered between lymphocytes. An in-depth exploration of the functions of B cells within these follicles suggested diverse roles and the activation of signaling pathways associated with antigen presentation and immune cell recruitment. These findings support the use of clinical *Mtb* HN878 strain for infection in mice as an appropriate model to study immune parameters associated with human TB granulomas.

Keywords. B-cell follicles; human granulomatous diseases; lung granuloma; *Mycobacterium tuberculosis* HN878; pulmonary tuberculosis.

Mycobacterium tuberculosis (*Mtb*) is a leading cause of death worldwide [1]. Animal models are valuable tools to identify correlates of protection and screen tuberculosis (TB) vaccine candidates. However, absence of accessible, cost-effective, and predictive mouse preclinical models that recapitulate clinical and histopathological features of human TB disease is a significant hurdle.

Granulomas, the hallmark of human TB disease, are characterized by a central core comprising infected neutrophils, alveolar macrophages, epithelioid macrophages, and giant multinucleated cells, surrounded by a peripheral cuff of lymphocytes [2]. Although tubercle granulomas may be protective, they may also serve as niches for bacterial persistence [3]. Indeed, heterogeneity in the morphology of human TB granulomas is observed [4]. Moreover, variations in the functional nature of individual granulomas can occur within infected macaques, a

nonhuman primate (NHP) model that closely reflects human TB disease and tubercle granulomas [5]. Localization of T cells expressing the C-X-C-chemokine receptor 5 (CXCR5) within organized B-cell clusters in mice and macaques promote the ability to form distinct lymphoid follicle containing granulomas that enable macrophages to control *Mtb* [6]. These observations highlight the importance of understanding the function of protective granulomas.

Ideally, discovery of immune parameters crucial for structural organization of protective granulomas must be performed in an animal model that mimics human granulomatous responses. Although mice do not fully develop human-like granulomas [7], NHPs, rabbits, and guinea pigs reliably mimic aspects of the human tubercle granulomas [7]. However, these larger animal models are more expensive in terms of the infrastructure and cost-effectiveness of experimentation. Thus, identifying mouse models of *Mtb* infection that generate granuloma features that closely resemble human tubercle granulomas would benefit the TB immunological and vaccine fields. Researchers have relied heavily on laboratory-adapted strains such as *Mtb* H37Rv and *Mtb* Erdman for infection in C57BL/6 (B6) inbred mice to study protective immunity. This is likely because *Mtb* H37Rv was the first genomically sequenced *Mtb* isolate [8]. In a recent study, we showed that use of clinical *Mtb* strains, such as W-Beijing

prototype HN878, can identify protective immune parameters not apparent in an *Mtb* H37Rv infection model [9–11]. In this study, we aimed to determine whether *Mtb* strain HN878 would also model morphological and immunological aspects of human tubercle granulomas. We show that *Mtb* HN878 infection in C57BL/6 mice, but not *Mtb* H37Rv infection, induced human-like granulomas in the lung, which we define as composed of a core of macrophages surrounded by a lymphocyte cuff, as well as formation of B-cell lymphoid follicles and germinal centers (GC) within tubercular granulomas. In addition, we validate this model by demonstrating that B cell-deficient mice, that are not more susceptible to *Mtb* H37Rv infection [6], are more susceptible to infection with *Mtb* HN878 infection. Thus, our novel findings support the utilization of clinical *Mtb* strains in experimental models to enhance the translational potential of experimental findings made in mice.

MATERIAL AND METHODS

Mice

The B6 and B6.129S2-*Ighm*^tm1Cgn^/J (*Ighm*^−/−^) mice were purchased from the Jackson Laboratory (Bar Harbor, ME) and bred at the Washington University School of Medicine in St. Louis animal facility. Six- to eight-week-old age- and sex-matched mice were used in accordance with the Institutional Animal Care and Use Committee guidelines at Washington University in St. Louis, approved under protocol 20160129.

Mycobacterium tuberculosis Infection

Mycobacterium tuberculosis H37Rv and HN878 were cultured in Proskauer Beck medium containing 0.05% Tween 80 to reach midlog phase and frozen in 1-mL aliquots at −80°C until used. Mice were aerosol infected with ~100 colony-forming units (CFUs) of the *Mtb* strains, using a Glas-Col airborne infection system [6]. Pulmonary bacterial burden was determined by plating serial dilutions of lung homogenates on 7H11 agar plates.

Specific pathogen-free (SPF), adult Indian rhesus macaques of both sexes were obtained from the Tulane National Primate Research Center, housed in an ABSL3 facility, and verified to be free of *Mtb* infection by tuberculin skin test. *Mycobacterium tuberculosis*-naive, SPF Indian rhesus macaques were exposed to aerosols of ~100 CFU *Mtb* Erdman as described earlier [6]. Animals exposed to the higher dose developed TB, as characterized by pyrexia, rapid weight loss, elevated serum C-reactive protein levels, high CXR scores, and detection of viable *Mtb* CFUs in the bronchoalveolar lavage fluid and were necropsied at 13 weeks.

Morphometric Analysis

Mouse and macaque lungs were infused with 10% neutral buffered formalin and embedded in paraffin. Five-micrometer lung sections were stained with hematoxylin and eosin and processed for light microscopy. For human TB histological studies, lung sections were obtained from participants with TB from the Tuberculosis Outpatient Clinic at the National Institute of Respiratory Diseases (INER) in Mexico City. Samples were obtained from participants before anti-*Mtb* treatment. All participants provided informed consent, and the study was approved by the Biomedical Research Ethics Committee of INER. Formalin-fixed and paraffin-embedded samples from humans and NHPs with pulmonary TB were processed as previously described [6]. Regions of human-like granulomas, lymphoid follicles, inflammatory infiltrates, and macrophage areas were delineated with the automated tool of the Zeiss Axioplan 2 microscope (Carl Zeiss), and average size in squared microns was calculated. For calculating area of inflamed lung sections, representative images were taken with the Hamamatsu Nanozoomer 2.0 HT system with NDP scan image acquisition software. Total area occupied by inflammation and total lung lobe area were quantified in a ×40 magnification. Percentage area occupied by inflammation was calculated by dividing the total area occupied by inflammation with the total lung lobe area.

Immunofluorescence

For immunofluorescence, lung sections were processed as described before [6] and probed with antibodies listed in Supplementary Table 1. Images were obtained with a Zeiss Axioplan 2 microscope and recorded with a Zeiss AxioCam digital camera. Area occupied by B-cell follicles was quantified by morphometric analysis using the morphometric tool of Zeiss Axioplan microscope.

In Situ Hybridization in Tissue

Expression of mouse CXCL13, interferon (IFN)-β, CCL2, and STAT-1 messenger ribonucleic acid (mRNA) in mouse lung sections were assessed by in situ hybridization using mouse riboprobes (RNAScope) as described before [6]. Images were visualized using an Olympus BX41 microscope and captured using a SPOT RT3 digital camera (Diagnostics Instruments Inc.).

Ribonucleic Acid-Sequence Processing and Analysis

After adapter trimming using Trimmomatic v0.36 [12], RNA-sequence (RNA-seq) reads were aligned to the mouse genome assembly (*Mus musculus* GRCm38; Ensembl release 91.0 [13]) using HISAT2 v2.1.0 [14]. Read fragments (read pairs or single reads) were quantified per gene per sample using featureCounts (version 1.5.1) [15]. The FPKM (fragments per kilobase of gene length per million reads mapped) normalization was also performed.

Significantly differentially expressed genes between lung and spleen sample sets were identified using DESeq2 (version 1.4.5) [16] with default settings and a minimum *P* value significance threshold of .05 (after false discovery rate [17] correction for the number of tests). Principal components analysis (PCA) was also calculated using DESeq2 output (default settings, using the top 500 most variable genes). Pathway enrichment analysis for

reactome [18] pathways among gene sets of interest was performed using the WebGestalt [19] web server.

Statistical Analysis

Differences between means of 2 groups were estimated using 2-tailed Student's *t* test in GraphPad Prism 5 (La Jolla, CA). *P* values ≤.05 were considered as significant.

RESULTS

Mycobacterium tuberculosis (*Mtb*) HN878 but Not *Mtb* H37Rv Infection Induced Human-Like Tuberculosis Lung Granulomas in Mice

To assess morphological characteristics of granulomas induced by clinical and laboratory-adapted *Mtb* strains, we infected B6 mice with low doses of either aerosolized *Mtb* HN878 or *Mtb* H37Rv. At different days postinfection (dpi), we assessed the structure and immune cell organization of the tubercle granuloma from HN878- and H37Rv-infected mice. *Mycobacterium tuberculosis* H37Rv-infected mice formed lesions in the lung characterized by disorganized conglomerates of foamy macrophages and epithelioid cells, dispersed between lymphoid follicles and occurring mainly at perivascular/peribronchial regions (Figure 1A). In contrast, *Mtb* HN878-induced lung lesions were distinguished by clearly defined tubercle granulomas, with a core of macrophages surrounded by a lymphocyte cuff, and were intercalated between areas of pneumonia (Figure 1B). Thus, *Mtb* HN878-induced tubercle granulomas, although lacking multinucleated cells, resemble classic granulomas found in human (Figure 1C, left panel) and macaques with pulmonary TB (Figure 1C, right panel).

Human-like granulomas were observed post *Mtb* HN878 infection in mice, and these were most abundant at day 50 (Figure 1D). Early stage HN878-induced granulomas displayed a well defined granuloma limited by a thin lymphocyte cuff (Supplementary Figure 1A). However, upon progression into chronic stages of disease, *Mtb* HN878-induced granulomas exhibited less-defined boundaries, more distinct lymphocyte cuff/localization, and a narrower central core (Supplementary Figure 1B–D). As the infection progressed, the number and size of human-like granulomas decreased (Figure 1D), being absorbed within extensive areas of tuberculous pneumonia (Supplementary Figure 1C). Phagocytic characteristics also changed over time. At day 50, epithelioid macrophages and neutrophils predominated, whereas foamy macrophages admixed with groups of epithelioid cells were characteristic at 100 dpi (Supplementary Figure 1B). Although *Mtb* HN878 is considered "hypervirulent" [20], except at early time points no significant differences in the lung area occupied by total inflammation or area occupied by macrophages in lungs of mice infected with either strain was observed (Supplementary Figure 2A and B). These data, taken together, suggest that *Mtb* HN878, but not *Mtb* H37Rv, induces lung human-like granulomas in mice and may be used to study organization of tubercle granulomas.

Mycobacterium tuberculosis HN878 Induced B-Cell Follicles and Germinal Centers Within Lung Human-Like Granulomas

B-cell lymphoid follicles within *Mtb*-infected lungs establishes protective immunity against *Mtb* through correct localization of CXCR5+ T cells into TB granulomas [6, 21]. Thus, we next determined *Mtb* strain-dependent changes in the formation of lymphoid follicles. *Mycobacterium tuberculosis* H37Rv elicited the formation of B-cell follicles scattered between conglomerates of T cells (Figure 2A, left upper panel) and areas of macrophages (Figure 2A, right upper panel), as previously described [6, 9, 21]. Meanwhile, *Mtb* HN878-induced human-like granulomas showed an enrichment of B cells at the peripheral lymphocyte cuff (Figure 2A, left lower panel), whereas the central core contained activated *Mtb*-carrying macrophages expressing inducible nitric oxide synthase (Figure 2A, right lower panel). It is interesting to note that *Mtb* HN878-induced human-like granulomas also expressed GC markers at the lymphocyte cuff (Figure 2B). These results demonstrate that immune features associated with effective *Mtb* control are also distributed within the human-like granulomas in *Mtb* HN878-infected lungs.

Given the protective role of B-cell follicles against *Mtb* [6, 9, 21], we estimated *Mtb* strain-dependent quantitative changes in the formation of lymphoid structures by morphometric analysis. These follicles arose closer to each other in *Mtb* HN878-infected lungs compared with those infected by *Mtb* H37Rv (Supplementary Figure 2C) at different dpi. We focused on lymphoid follicle formation at 50 dpi, when the most significant histopathological differences between *Mtb* HN878 and *Mtb* H37Rv occurred. Morphometric analysis revealed no discrepancies in the amount of B-cell follicles induced by the different strains, but the average size and lung area occupied by B-cell follicles was greater in *Mtb* HN878-infected mice (Figure 2C). These findings show that the spatial pattern and magnitude of lymphoid tissue induction differ between clinical and laboratory-adapted *Mtb* strains.

Development of B-cell lymphoid follicles depends on the expression of the chemokine CXCL13, which is crucial for the recruitment of CXCR5+ T cells, B-cell follicle formation, and *Mtb* control [6]. We observed that *Mtb* H37Rv induced the formation of lymphoid follicles and CXCL13 expression throughout the follicles (Figure 3A, left column). In sharp contrast, CXCL13 mRNA expression localized specifically within the lymphocyte zones of HN878-infected lung granulomas (Figure 3A, right column). In addition, CCL-2 mRNA expression was similar in H37Rv and HN878-infected lung granulomas (Figure 3B). Consistent with previous data, HN878 infection resulted in robust IFN-β mRNA within the lung, predominantly outside the lymphocytic areas (Figure 3C) [22]. Finally, STAT1 mRNA expression, although increased upon HN878 infection, was localized within the lymphoid areas in both H37Rv and HN878 infection (Figure 3D). Taken together, these data suggest that HN878 infection promotes the localized expression of CXCL-13 to mediate the formation of lymphoid structures in the lung.
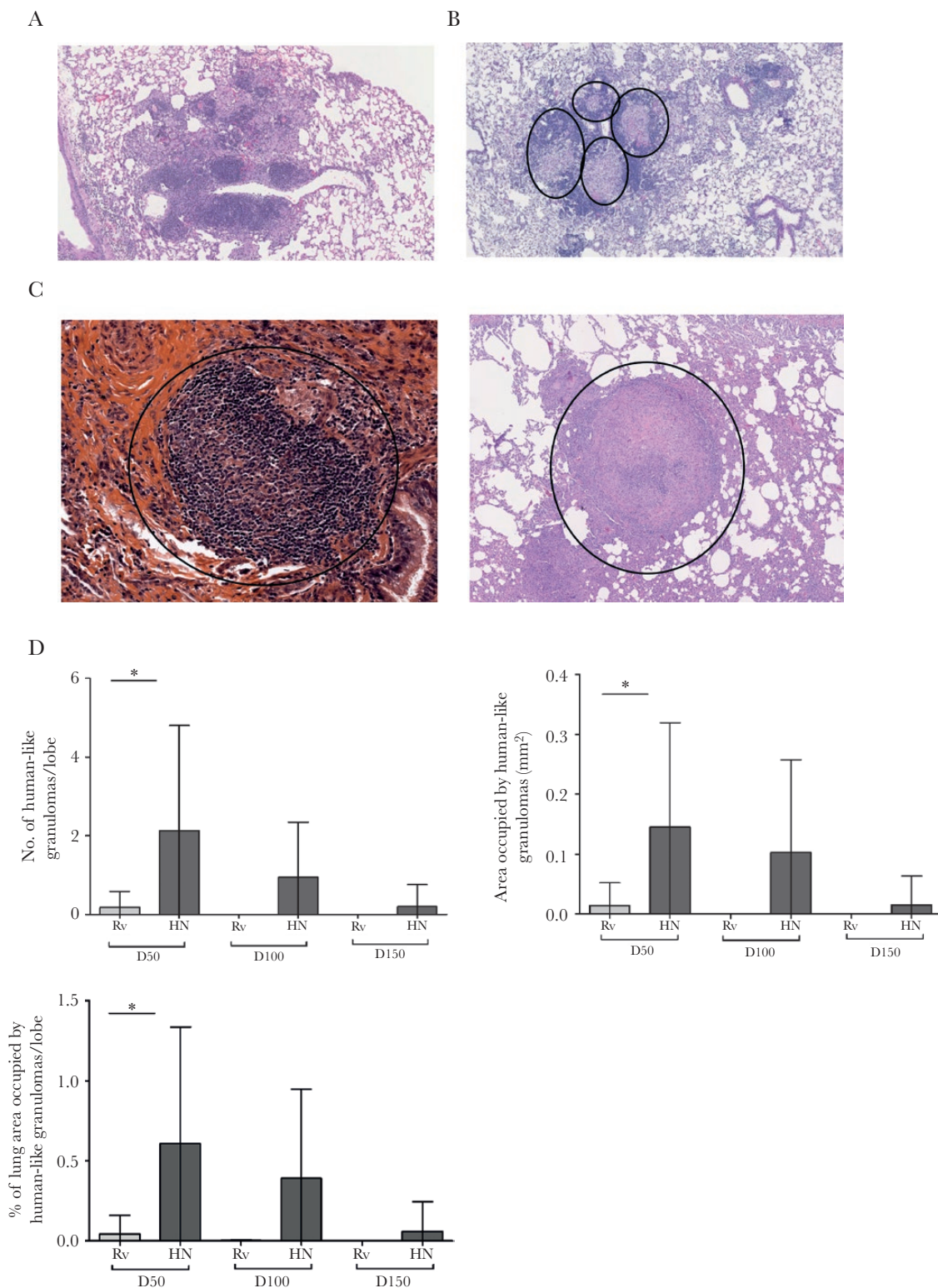
Figure 1. *Mycobacterium tuberculosis* (*Mtb*) HN878 infection induces human-like TB granulomas in lungs of mice. (A and B) C57BL/6 mice were aerosol infected with ~100 colony-forming units of *Mtb* H37Rv (Rv) or *Mtb* HN878 (HN) and sacrificed at 50, 100, and 150 days postinfection (dpi). Formalin-fixed and paraffin-embedded (FFPE) lung sections were stained with hematoxylin and eosin, and samples were histologically assessed. (A) The Rv infection is representative at 50 dpi. (B) The HN infection is representative of 50 dpi. (C) Human biopsy specimen obtained from pulmonary tuberculosis (TB) patient (left panel) and nonhuman primates with pulmonary TB that were infected with *Mtb* Erdman (right panel, 13 weeks postinfection). (D) The number of human-like granulomas per mouse lung lobe was determined histologically in FFPE lung sections. Area occupied by human-like granulomas quantified using the morphometric tool of the Zeiss Axioplan microscope. Percentage from lung area occupied by human-like granulomas per mouse lung lobe was determined. The data shown represent mean (±standard deviation) values from 2 to 3 independent experiments per time point (n = 4–5 mice per group in each experiment). Student *t* test was used to determine differences per time point. *, *P* < .05.

A

B

Rv

CD3 B220   iNOS *Mtb* B220   PNA PCNA B220

HN

C
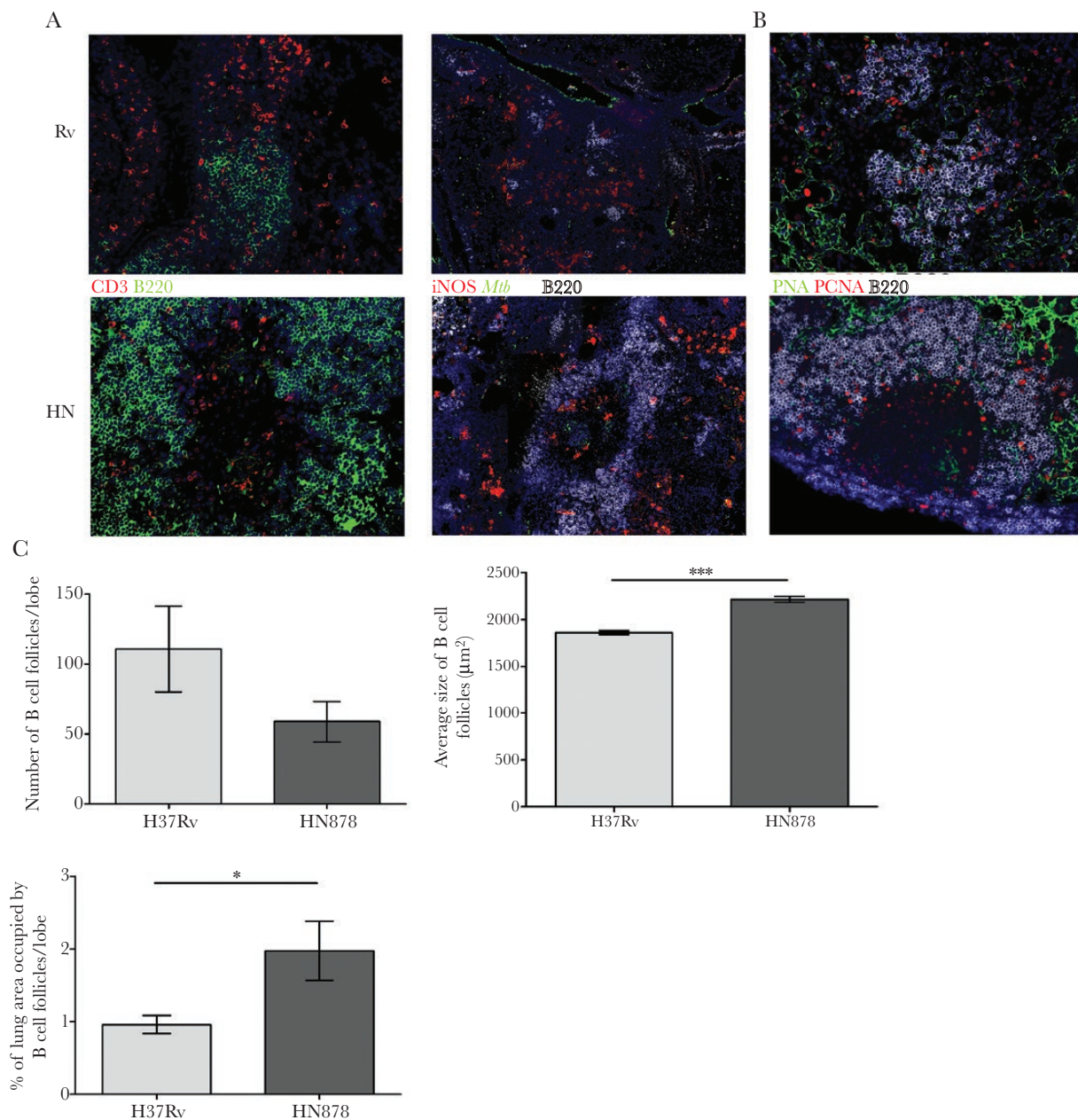
Figure 2. HN878 infection induces robust B-cell lymphoid follicle formation within human-like granulomas. C57BL/6 mice were infected with *Mycobacterium tuberculosis* (*Mtb*) H37Rv (Rv) or *Mtb* HN878 (HN) as described in Figure 1. (A) B-cell lymphoid follicles were stained using antibodies to CD3 and B220, and *Mtb* localization with inducible nitric oxide synthase (iNOS)-expressing macrophages was also stained. (B) Expression of germinal center follicles within granulomas was assessed by B220/PCNA/PNA staining. (C) At 50 days postinfection, the total number of B-cell follicles, the size of each individual B-cell follicle, and the percentage of the lung area occupied by B-cell follicles per lobe were quantified using the morphometric tool of the Zeiss Axioplan microscope. The data represented are mean (±standard deviation) values from 2 to 3 independent experiments (n = 5 mice in each HN878 experiment, n = 3–4 mice in H37Rv experiments). Student *t* test was used to determine differences between the groups. *, $P < .05$; ***, $P < .0001$.

B Cells Play a Specific Protective Role During HN878 Infection but Not H37Rv Infection

To better characterize the role of these B-cell follicles, we infected B6 and *Ighm*$^{-/-}$ mice deficient in B cells with aerosolized *Mtb* HN878. In a previous study, infection of *Ighm*$^{-/-}$ mice with H37Rv and Erdman did not result in increased susceptibility to infection [6]. However, when infected with the HN878 strain, there was a significant increase in lung bacterial burden in *Ighm*$^{-/-}$ mice during the course of infection, when compared with B6 mice (Figure 4A). Furthermore, HN878 strain infection enhanced lung inflammation in *Ighm*$^{-/-}$ when compared with B6 mice at 50 dpi (Figure 4B). Absence of B cells during Erdman and H37Rv low-dose infection does not impact *Mtb* control as shown before [6, 23] and shown here (Figure 4C). In addition,
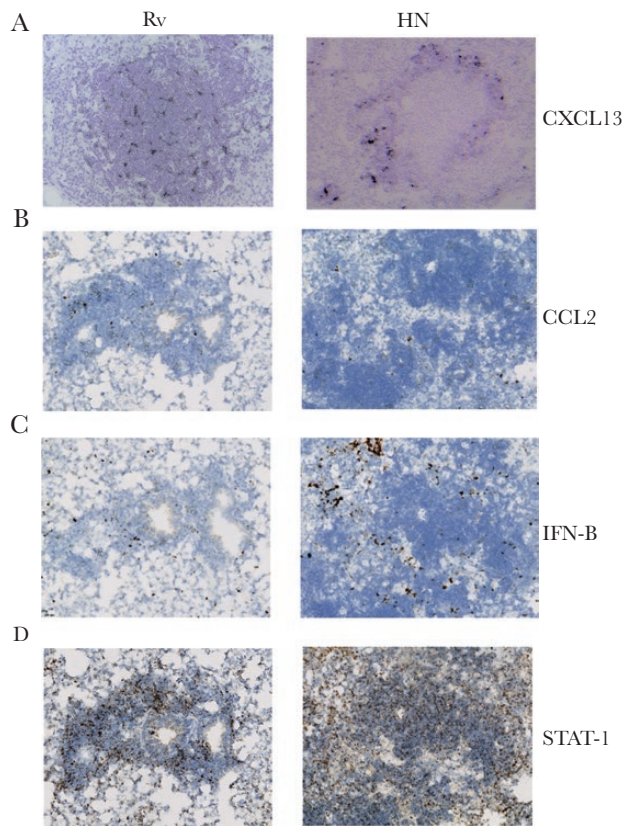
Figure 3. HN878 infection induces differential expression of cytokines and chemokines around lung granulomas. C57BL/6 mice were infected with *Mycobacterium tuberculosis* (*Mtb*) H37Rv (Rv) or *Mtb* HN878 (HN) as described in Figure 1. (A) The expression of CXCL13, (B) STAT-1, (C) CCL2, and (D) interferon-β (IFN-B) was determined by in situ hybridization of messenger ribonucleic acid on formalin-fixed and paraffin-embedded slides.

despite the increased inflammation observed in the lungs of HN878-infected *Ighm*$^{-/-}$ mice, we observed reduced accumulation of CXCR5-expressing T cells within the granulomas (Figure 4D). Similar reduction in accumulation of CXCR5-expressing T cells were obtained in the lungs of H37Rv-infected *Ighm*$^{-/-}$ mice when compared with its B6 control (Figure 4D). Thus, HN878 infection results in increased *Mtb* CFU as well as increased inflammation, suggesting a protective and anti-inflammatory role for B cells in *Mtb* HN878 infection.

We next investigated the genes and pathways upregulated in highly purified lung B cells during infection compared with B cells isolated from the spleen of *Mtb*-infected mice. The RNA-Seq samples clustered according to the location of isolated lung or splenic B cells by PCA (Supplementary Figure 3). In the lung B cells, 1950 genes were significantly more highly expressed, and 1932 genes were significantly more highly expressed in the splenic B cells. The top 20 genes from each of these lists are shown in Table 1 and Supplementary Table 2, respectively. Significantly enriched pathways among these differentially expressed genes are shown in Table 2 and Supplementary Table 3, respectively. The most differentially upregulated gene in lung

B cells was Surfactant Associated Protein C, *Sftpc*, with a 12.62 log$_2$ fold change. Among reactome pathways, the most enriched pathways converged on the Toll-like receptor (TLR) cascades, transforming growth factor (TGF)-β signaling, endocytosis, and major histocompatibility complex (MHC) class II antigen presentation. In contrast, pathways enriched in the splenic B cells were related to the deoxyribonucleic acid replication, cell cycle checkpoints, and cell replication components, with upregulated genes such as Kinesin Family Member 20A (*Kif20a*) and PCNA Clamp Associated Factor (*Pclaf*). Taken together, our data provide novel insights into the association of B cells induced after *Mtb* infection with antigen presentation and TGF-β signaling.

DISCUSSION

Animal models aid to mechanistically understand the basis of TB disease pathogenesis. Development of cost-effective and tractable small animal models that closely mimic human TB disease would benefit the field. In this study, we show that the clinical *Mtb* strain, HN878, as an infection model in B6 mice can induce anatomical and immune structures that resemble human-like granulomas. The human-like granulomas in HN878-infected B6 mice also exhibit distinct formation of lymphoid follicles and surround macrophage areas, similar to human and NHP-like TB granulomas. We demonstrate a protective and anti-inflammatory role for B cells in controlling *Mtb* HN878 infection. These findings, coupled with our previous work on dissecting the roles of CXCR5, CCR2, and interleukin (IL)-17 in HN878 infection, project the use of hypervirulent HN878 strain as more appropriate, than use of laboratory-adapted strains, to study immune parameters that participate in TB granuloma formation, as seen clinically [9–11].

In a previous study, Tsai et al [2] characterized the kinetics of granuloma formation in human and B6 mice infected with *Mtb* Erdman strain, and they showed that in mice, granulomas were characterized by distinct B-cell macrophage areas, whereas in human TB granulomas, macrophage areas were surrounded by B-cell aggregates that also contained CD3$^+$ T cells. However, in our study, when B6 mice were infected with *Mtb* HN878, the TB granulomas consisted of *Mtb*-infected macrophages surrounded by B and T cells, a characteristic feature of human lesions [6]. It is interesting to note that we also observed a steady increase in the number of foamy macrophages as disease progressed. These results are consistent with studies by Ordway et al [20] who showed that *Mtb* HN878-infection induced the presence of foamy macrophages in lungs and that granulomatous lesions continued to increase in size and were characterized over time by large coalescing inflammatory granulomas. In contrast, we found that early, well defined human-like granulomas were absorbed between areas of alveolar consolidation over time. Thus, although the dynamics of the granulomatous lesions differ with the findings of Ordway et al [20], the outcome concurs in both studies. Furthermore, our observations coincide with
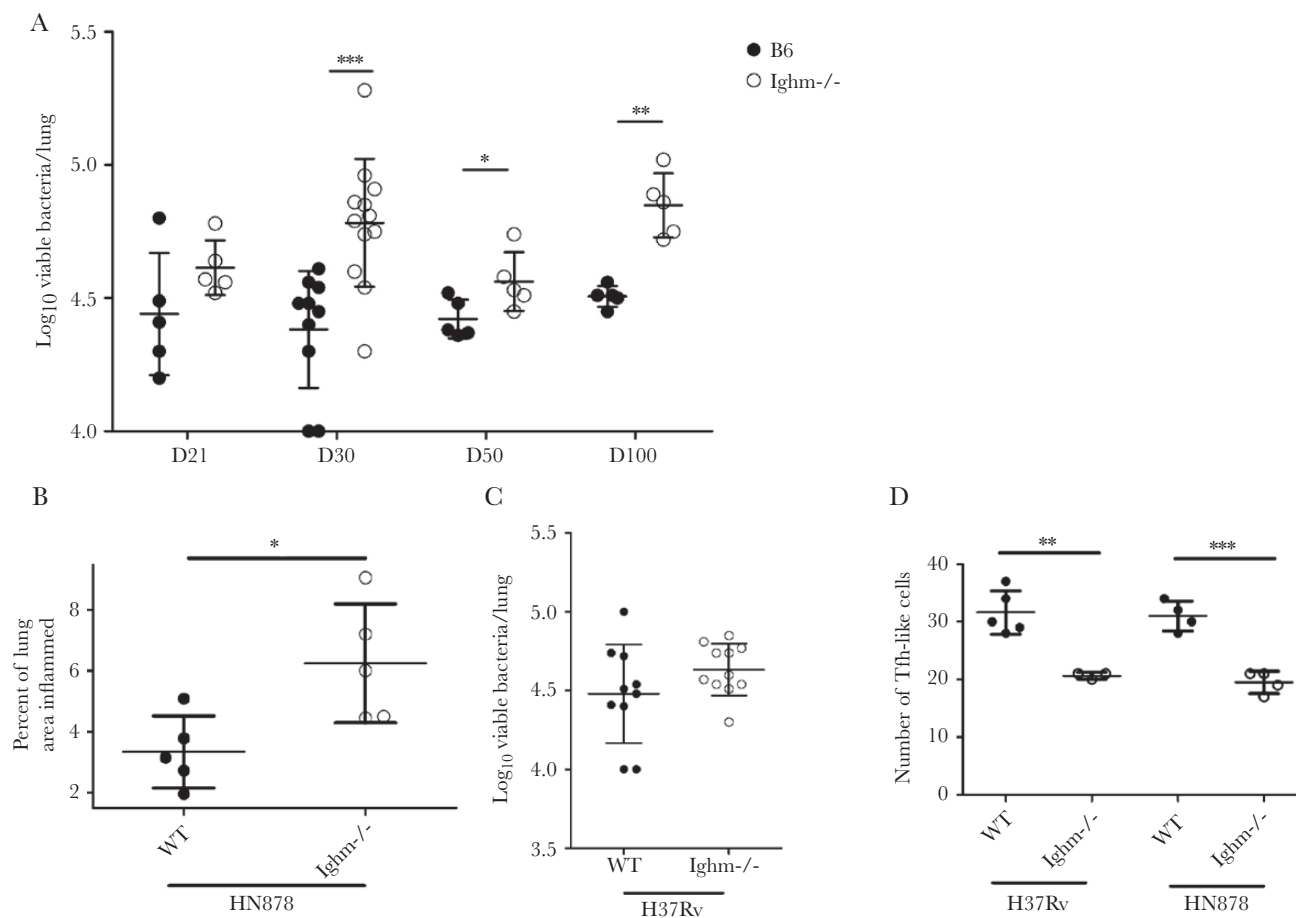
Figure 4. B-cell deficient mice show increased susceptibility to HN878 infection. C57BL/6 (B6) and *Ighm–/–* mice were aerosol infected with ~100 colony-forming units (CFUs) of *Mycobacterium tuberculosis* (*Mtb*) H37RV or *Mtb* HN878. (A) Bacterial burden in the lung of B6 and *Ighm–/–* HN-infected animals was determined at different days postinfection (dpi) after plating and counting CFUs and used as a measure of susceptibility to HN infection between B6 and *Ighm–/–* mice. (B) The percentage of inflamed lung area was determined histologically in formalin-fixed and paraffin-embedded lung sections. Area occupied inflammation was quantified using the Nanozoomer software. Percentage from lung area occupied by inflammation per mouse lung was determined. (C) Bacterial burden in the lung of B6 and *Ighm–/–* Rv-infected animals was determined at 50 dpi after plating and counting CFUs and used as a measure of susceptibility to Rv infection between B6 and *Ighm–/–* mice. (D) At 50 dpi, the number of T cells around granulomas in B6 and *Ighm–/–* mice infected with Rv or HN was quantified in a ×200 field of view using the morphometric tool of the Zeiss Axioplan microscope after staining using antibodies to CD3 and CXCR5. (A–D) The data shown represent mean (±standard deviation) values from 1 to 3 independent experiments per time point (n = 4–5 mice per group in each experiment). Student *t* test was used to determine differences per time point. *, $P < .05$; **, $P < .005$; ***, $P < .0005$.

other reports using different strains from the W-Beijing lineage [24] and resemble morphology of lung samples from humans with postprimary TB described before the advent of anti-TB drugs [25]. This finding of alveolar consolidation at late time points of infection poses a potential caveat for examining late time points of *Mtb* HN878 infection to study protective spatial patterns of interplay between leukocytes forming granulomas. The abundance of B cells in human-like granulomas of HN878-infected mice suggests a role in immunity against emerging clinical *Mtb* strains [6, 7, 21]. Moreover, active production of CXCL13, a chemokine crucial for correct localization of B and T cells within lymphoid follicles, in *Mtb* HN878-induced mouse granulomas, indicates that mechanisms of protection discovered for laboratory-adapted strains are also relevant to control hypervirulent *Mtb* in murine models [6]. Nonetheless, the spatial pattern and magnitude of lymphoid tissue induction

may differ between bacterial genotypes potentially impacting bacterial pathogenicity. On the other hand, despite a decrease in clearly defined human-like granulomas during later stages of HN878 infection, *Mtb* CFU was not altered. Taken together, these data, although supporting the idea that HN878 infection in mice is a tractable model to study immune features of protection, suggest that such features may not be directly linked to *Mtb* CFU control at the level of the granuloma.

Maglione et al [23] showed that *Mtb* infection with a high dose of *Mtb* Erdman increased bacterial burden and exacerbated pulmonary inflammation in B cell-deficient mice. Our results show decreased *Mtb* control and increased inflammation while using a physiologically relevant dose with the clinically relevant HN878 strain. These results support the importance of a protective and anti-inflammatory role of B cells in *Mtb* control. It is known that B cells produce

Table 1. The Top 50 Genes Most Significantly Overexpressed in the Lung B Cells Relative to the Spleen B Cells

Gene Name	Gene Description	Average Expression Level (FPKM)		Log$_2$ Fold Change	P Value
		Spleen	Lung		
Atf3	Activating transcription factor 3	0.58	41.97	−6.30	3.8E-225
Ccr7	Chemokine (C-C motif) receptor 7	187.99	1078.24	−2.65	6.1E-150
Pmaip1	Phorbol-12-myristate-13-acetate-induced protein 1	11.99	62.85	−2.52	1.3E-149
Siah2	7 in absentia 2	15.11	69.93	−2.34	1.7E-119
Nr4a1	Nuclear receptor subfamily 4, group A, member 1	19.64	631.62	−5.14	2.7E-113
Tgif1	TGFβ-induced factor homeobox 1	14.00	51.82	−2.02	1.7E-105
Rgcc	Regulator of cell cycle	2.95	67.69	−4.66	1.5E-97
Dusp5	Dual specificity phosphatase 5	2.85	30.75	−3.57	9.0E-95
Pnrc1	Proline-rich nuclear receptor coactivator 1	150.68	423.37	−1.62	1.4E-91
Vps37b	Vacuolar protein sorting 37B	15.66	83.48	−2.54	1.3E-85
Trib1	Tribbles pseudokinase 1	3.73	14.15	−2.05	2.6E-80
Lmna	Lamin A	0.91	10.94	−3.72	7.2E-79
Rel	Reticuloendotheliosis oncogene	21.24	71.46	−1.88	3.6E-77
Bambi	BMP and activin membrane-bound inhibitor	0.84	13.15	−4.09	5.7E-74
Ifrd1	Interferon-related developmental regulator 1	8.97	30.52	−1.90	1.6E-73
B3gnt7	UDP-GlcNAc:betaGal beta-1,3-N-acetylglucosaminyltransferase 7	1.57	10.29	−2.85	2.9E-65
Tnfaip3	Tumor necrosis factor, alpha-induced protein 3	10.47	43.79	−2.20	4.0E-64
Cdkn1a	Cyclin-dependent kinase inhibitor 1A (P21)	1.52	12.81	−3.21	2.2E-63
Pim3	Proviral integration site 3	25.03	104.66	−2.19	1.1E-62
Crem	cAMP responsive element modulator	3.21	11.26	−1.94	7.6E-57
Cdt1	Chromatin licensing and DNA replication factor 1	22.07	58.78	−1.54	8.7E-54
Cystm1	Cysteine-rich transmembrane module containing 1	0.19	3.53	−4.37	9.4E-52
Sik1	Salt inducible kinase 1	9.64	44.36	−2.33	9.4E-50
Zbtb10	Zinc finger and BTB domain containing 10	0.54	4.61	−3.22	2.0E-48
Hspa2	Heat shock protein 2	7.83	24.78	−1.79	2.4E-48
Oser1	Oxidative stress responsive serine rich 1	23.97	69.74	−1.67	8.8E-46
Stk17b	Serine/threonine kinase 17b (apoptosis-inducing)	69.85	261.24	−2.03	9.3E-45
Klf6	Kruppel-like factor 6	72.56	331.20	−2.33	6.4E-44
Tubb2a	Tubulin, beta 2A class IIA	5.12	16.65	−1.83	1.0E-43
Zfp622	Zinc finger protein 622	34.50	76.63	−1.28	8.6E-41
Nfil3	Nuclear factor, interleukin 3, regulated	0.63	5.62	−3.32	1.4E-40
Rnf125	Ring finger protein 125	1.01	8.19	−3.15	2.1E-40
Atg101	Autophagy related 101	62.99	156.49	−1.44	6.6E-40
Map1lc3a	Microtubule-associated protein 1 light chain 3 alpha	14.02	37.19	−1.54	7.7E-40
Plaur	Plasminogen activator, urokinase receptor	87.26	361.81	−2.18	1.2E-39
Ets2	E26 avian leukemia oncogene 2, 3' domain	4.59	14.06	−1.75	1.9E-39
Cd69	CD69 antigen	40.00	127.30	−1.80	2.2E-39
Ypel5	Yippee-like 5 (*Drosophila*)	32.67	82.38	−1.46	1.3E-38
Irf2bp2	Interferon regulatory factor 2 binding protein 2	7.69	26.37	−1.91	1.7E-38
Sftpc	Surfactant-associated protein C	0.00	45.56	−12.62	5.3E-38
Nr4a2	Nuclear receptor subfamily 4, group A, member 2	0.15	2.69	−4.31	6.2E-37
Gem	GTP binding protein (gene overexpressed in skeletal muscle)	49.42	147.32	−1.71	1.0E-36
Dusp4	Dual specificity phosphatase 4	3.20	17.45	−2.58	7.1E-36
1700017B05Rik	RIKEN cDNA 1700017B05 gene	12.16	31.06	−1.48	9.2E-36
Dnajb9	DnaJ heat shock protein family (Hsp40) member B9	28.22	101.66	−1.98	1.5E-35
Plk2	Polo-like kinase 2	9.82	225.40	−4.66	3.4E-35
Litaf	LPS-induced TN factor	19.78	77.89	−2.11	4.8E-35
Yrdc	yrdC domain containing (*Escherichia coli*)	38.57	78.94	−1.16	2.4E-34
Cd83	CD83 antigen	423.01	1747.63	−2.18	2.8E-34
Dennd4a	DENN/MADD domain containing 4A	6.34	16.62	−1.52	5.6E-34

Abbreviations: cAMP, cyclic adenine monophosphate; DNA, deoxyribonucleic acid; FPKM, fragments per kilobase of gene length per million reads mapped; LPS, lipopolysaccharide; TGFβ, transforming growth factor beta; TN, tumor necrosis.

Table 2. Significantly Enriched Reactome Pathways Among the 1950 Genes Significantly Overexpressed in the Lung B Cells Relative to the Spleen B Cells

Pathway Description	Number of Overexpressed Genes	Total Number of Genes	FDR-Adjusted P Value
mRNA Splicing	43	171	5.7E-05
Posttranslational protein modification	201	1321	5.7E-05
RAF-independent MAPK1/3 activation	13	23	5.7E-05
Processing of Capped Intron-Containing Pre-mRNA	51	224	6.0E-05
Immune System	240	1649	6.0E-05
mRNA Splicing—Major Pathway	40	163	1.1E-04
Signaling by TGF-β Receptor Complex	21	60	1.1E-04
Vesicle-mediated transport	105	608	1.1E-04
Toll-Like Receptor 4 (TLR4) Cascade	30	107	1.1E-04
Adaptive Immune System	115	690	1.7E-04
Membrane Trafficking	99	573	1.8E-04
Downregulation of SMAD2/3:SMAD4 transcriptional activity	11	20	2.0E-04
Golgi-Associated Vesicle Biogenesis	18	51	3.5E-04
MyD88-independent TLR4 cascade	25	87	3.5E-04
TRIF(TICAM1)-mediated TLR4 signaling	25	87	3.5E-04
trans-Golgi Network Vesicle Budding	21	67	4.1E-04
Clathrin-derived vesicle budding	21	67	4.1E-04
Negative regulation of MAPK pathway	15	39	5.5E-04
Toll-Like Receptor 10 (TLR10) Cascade	21	70	7.2E-04
Toll-Like Receptor 5 (TLR5) Cascade	21	70	7.2E-04
MyD88 cascade initiated on plasma membrane	21	70	7.2E-04
Toll-Like Receptor 7/8 (TLR7/8) Cascade	22	76	7.2E-04
MyD88-dependent cascade initiated on endosome	22	76	7.2E-04
MyD88:MAL(TIRAP) cascade initiated on plasma membrane	21	71	7.2E-04
Toll-Like Receptor TLR1:TLR2 Cascade	21	71	7.2E-04
Toll-Like Receptor TLR6:TLR2 Cascade	21	71	7.2E-04
Toll-Like Receptor 2 (TLR2) Cascade	21	71	7.2E-04
Toll-Like Receptor 3 (TLR3) Cascade	20	67	9.6E-04
Transcriptional activity of SMAD2/SMAD3:SMAD4 heterotrimer	14	38	1.2E-03
TRAF6 mediated induction of NFkB and MAP kinases upon TLR7/8 or 9 activation	21	74	1.3E-03
Toll-Like Receptor 9 (TLR9) Cascade	22	80	1.4E-03
Clathrin-mediated endocytosis	31	134	1.6E-03
Toll-Like Receptor Cascades	33	147	1.7E-03
Metabolism of proteins	222	1619	2.3E-03
MHC class II antigen presentation	28	119	2.5E-03
Innate Immune System	139	948	3.8E-03
Signaling by TGF-β family members	22	87	4.7E-03
Cleavage of Growing Transcript in the Termination Region	17	59	4.7E-03
RNA Polymerase II Transcription Termination	17	59	4.7E-03
Cargo recognition for clathrin-mediated endocytosis	23	96	7.3E-03
SUMOylation of transcription cofactors	12	35	7.4E-03

Abbreviations: FDR, false discovery rate; MHC, major histocompatibility complex; mRNA, messenger ribonucleic acid; TGF, transforming growth factor.

anti-inflammatory cytokines such as IL-10 that control lung inflammation in fungal infections [26]. We propose this B-cell function as a possible mechanism to be further explored in *Mtb* infection.

We found upregulation of *Sftpc* and *Ccr7* in enriched lung B cells from *Mtb*-infected mice. Because the gene product of *Sftpc* is a hydrophobic surfactant protein, it would not be unusual for the gene to be highly upregulated in cells found in the lung with its expression primarily reported in lung epithelial cells [27, 28]. However, what is of interest is finding this gene expressed in B cells. Although we did not compare the magnitude of expression between lung epithelial cells and lung B cells, our work suggests that, after *Mtb* infection, unexpected cell types can also express *Sftpc*. CCR7 is an important chemokine that is relevant for B-cell follicular development in the lungs [29]. Consistent with this, lung B cells expressed high levels of CCR7 mRNA, likely allowing for homing of these immune cells into lymphoid follicles. In addition, we have reported that mice deficient in CCL19/CCL21 production, the ligands for the CCR7 receptor, are more susceptible to *Mtb* infection [30]. Thus, the importance of the CCR7-CCL19/21 signaling axis is appreciated.

It is interesting to note that the most enriched reactome pathways appear to converge on TLRs, endocytosis, and TGF-β. Previous studies have shown the importance of TLR2 signaling in B cells as a potential correlate of protection because blocking this signal led to a reduction of activation markers when exposed to whole cell *Mtb* lysate [31]. Likewise, phagocytic capabilities and immune activation in human B cells through upregulated MHC class II presentation has also been identified [32]. The importance of MHC class II presentation for B-cell migration into GCs is through assistance from T follicular helper cells [33]. Our results corroborate these findings and suggest a robust role of B cells in the containment of *Mtb* through a combination of these potential mechanisms. Moreover, our results suggest an expanded role of TLR signaling, beyond the formerly described TLR2 cascade, in the context of *Mtb* infection that remains to be explored. Concerning the splenic B cells' expression profiles, the focus on the cell cycle is not to suggest that the lung B cells lack cell cycle activity, but that the immune activation discussed above in the lung is more active, which causes cell cycle genes to appear relatively underexpressed relative to splenic B cells. Thus, the comparison of splenic B cells with lung B cells provides a novel look at the transcriptional profile of B cells in response to *Mtb* infection and suggests their potential role in orchestrating a protective immune response.

CONCLUSIONS

In summary, the spectrum of histopathological differences attributed to the TB granuloma necessitates the development and utilization of different animal models. Our findings support a shift towards the use of clinically relevant hypervirulent *Mtb* strains in immunocompetent mice as an additional accessible model that better emulates the histopathology of human TB to study parameters associated with formation of protective granulomas and B-cell follicles.

Supplementary Data

Supplementary materials are available at *The Journal of Infectious Diseases* online. Consisting of data provided by the authors to benefit the reader, the posted materials are not copyedited and are the sole responsibility of the authors, so questions or comments should be addressed to the corresponding author.

Notes

Potential conflicts of interest. All authors: No reported conflicts of interest. All authors have submitted the ICMJE Form for Disclosure of Potential Conflicts of Interest.

References

1. Global Tuberculosis Report 2019. World Health Organization **2019**; https://www.who.int/tb/publications/global_report/en/

2. Tsai MC, Chakravarty S, Zhu G, et al. Characterization of the tuberculous granuloma in murine and human lungs: cellular composition and relative tissue oxygen tension. Cell Microbiol **2006**; 8:218–32.

3. Silva Miranda M, Breiman A, Allain S, Deknuydt F, Altare F. The tuberculous granuloma: an unsuccessful host defence mechanism providing a safety shelter for the bacteria? Clin Dev Immunol **2012**; 2012:139127.

4. Lenaerts A, Barry CE 3rd, Dartois V. Heterogeneity in tuberculosis pathology, microenvironments and therapeutic responses. Immunol Rev **2015**; 264:288–307.

5. Lin PL, Ford CB, Coleman MT, et al. Sterilization of granulomas is common in active and latent tuberculosis despite within-host variability in bacterial killing. Nat Med **2014**; 20:75–9.

6. Slight SR, Rangel-Moreno J, Gopal R, et al. CXCR5+ T helper cells mediate protective immunity against tuberculosis. J Clin Invest **2013**; 123:712–26.

7. Via LE, Lin PL, Ray SM, et al. Tuberculous granulomas are hypoxic in guinea pigs, rabbits, and nonhuman primates. Infect Immun **2008**; 76:2333–40.

8. Cole ST, Brosch R, Parkhill J, et al. Deciphering the biology of *Mycobacterium tuberculosis* from the complete genome sequence. Nature **1998**; 393:537–44.

9. Gopal R, Monin L, Slight S, et al. Unexpected role for IL-17 in protective immunity against hypervirulent *Mycobacterium tuberculosis* HN878 infection. PLoS Pathog **2014**; 10:e1004099.

10. Domingo-Gonzalez R, Das S, Griffiths KL, et al. Interleukin-17 limits hypoxia-inducible factor 1alpha and development of hypoxic granulomas during tuberculosis. JCI Insight **2017**; 2:e92973.

11. Dunlap MD, Howard N, Das S, et al. A novel role for C-C motif chemokine receptor 2 during infection with hypervirulent *Mycobacterium tuberculosis*. Mucosal Immunol **2018**; 11:1727–42.

12. Bolger AM, Lohse M, Usadel B. Trimmomatic: a flexible trimmer for Illumina sequence data. Bioinformatics **2014**; 30:2114–20.

13. Zerbino DR, Achuthan P, Akanni W, et al. Ensembl 2018. Nucleic Acids Res **2018**; 46:D754–61.

14. Kim D, Langmead B, Salzberg SL. HISAT: a fast spliced aligner with low memory requirements. Nat Methods **2015**; 12:357–60.

15. Liao Y, Smyth GK, Shi W. featureCounts: an efficient general purpose program for assigning sequence reads to genomic features. Bioinformatics **2014**; 30:923–30.

16. Anders S, Huber W. Differential expression analysis for sequence count data. Genome Biol **2010**; 11:R106.

17. Benjamini Y, Hochberg Y. Controlling the false discovery rate: a practical and powerful approach to multiple testing. J R Stat Soc Series B Stat Methodol **1995**; 57:289–300.

18. Fabregat A, Jupe S, Matthews L, et al. The reactome pathway knowledgebase. Nucleic Acids Res **2018**; 46:D649–55.

19. Wang J, Vasaikar S, Shi Z, Greer M, Zhang B. WebGestalt 2017: a more comprehensive, powerful, flexible and interactive gene set enrichment analysis toolkit. Nucleic Acids Res **2017**; 45:W130–7.

20. Ordway D, Henao-Tamayo M, Harton M, et al. The hypervirulent *Mycobacterium tuberculosis* strain HN878 induces a potent TH1 response followed by rapid downregulation. J Immunol **2007**; 179:522–31.

21. Monin L, Griffiths KL, Slight S, Lin Y, Rangel-Moreno J, Khader SA. Immune requirements for protective Th17 recall responses to *Mycobacterium tuberculosis* challenge. Mucosal Immunol **2015**; 8:1099–109.

22. Manca C, Tsenova L, Bergtold A, et al. Virulence of a *Mycobacterium tuberculosis* clinical isolate in mice is determined by failure to induce Th1 type immunity and is associated with induction of IFN. Proc Natl Acad Sci U S A **2001**; 98:5752–7.

23. Maglione PJ, Xu J, Chan J. B cells moderate inflammatory progression and enhance bacterial containment upon pulmonary challenge with *Mycobacterium tuberculosis*. J Immunol **2007**; 178:7222–34.

24. Almeida FM, Ventura TL, Amaral EP, et al. Hypervirulent *Mycobacterium tuberculosis* strain triggers necrotic lung pathology associated with enhanced recruitment of neutrophils in resistant C57BL/6 mice. PLoS One **2017**; 12:e0173715.

25. Hunter RL. Tuberculosis as a three-act play: a new paradigm for the pathogenesis of pulmonary tuberculosis. Tuberculosis (Edinb) **2016**; 97:8–17.

26. Liu F, Lu X, Dai W, et al. IL-10-producing B cells regulate T helper cell immune responses during 1,3-β-glucan-induced lung inflammation. Front Immunol **2017**; 8:414.

27. Bridges JP, Wert SE, Nogee LM, Weaver TE. Expression of a human surfactant protein C mutation associated with interstitial lung disease disrupts lung development in transgenic mice. J Biol Chem **2003**; 278:52739–46.

28. Kalina MM, Mason RJ, Shannon JM. Surfactant protein C is expressed in alveolar type II cells but not in clara cells of rat lung. Am J Respir Cell Mol Biol **1992**; 6:594–600.

29. Kahnert A, Höpken UE, Stein M, Bandermann S, Lipp M, Kaufmann SH. *Mycobacterium tuberculosis* triggers formation of lymphoid structure in murine lungs. J Infect Dis **2007**; 195:46–54.

30. Khader SA, Rangel-Moreno J, Fountain JJ, et al. In a murine tuberculosis model, the absence of homeostatic chemokines delays granuloma formation and protective immunity. J Immunol **2009**; 183:8004–14.

31. Helbig S, Rekhtman S, Dostie K, et al. B cell responses in older adults with latent tuberculosis: considerations for vaccine development. Glob Vaccines Immunol **2016**; 1:44–52.

32. Zhu Q, Zhang M, Shi M, et al. Human B cells have an active phagocytic capability and undergo immune activation upon phagocytosis of *Mycobacterium tuberculosis*. Immunobiology **2016**; 221:558–67.

33. Draghi NA, Denzin LK. H2-O, a MHC class II-like protein, sets a threshold for B-cell entry into germinal centers. Proc Natl Acad Sci U S A **2010**; 107:16607–12.